Global Survey and Statistics of Radio-Frequency Interference in AMSR-E Land Observations

Eni G. Njoku, *Fellow, IEEE*, Peter Ashcroft, Tsz K. Chan, *Senior Member, IEEE*, and Li Li, *Member, IEEE*

Abstract—Radio-frequency interference (RFI) is an increasingly serious problem for passive and active microwave sensing of the Earth. To satisfy their measurement objectives, many spaceborne passive sensors must operate in unprotected bands, and future sensors may also need to operate in unprotected bands. Data from these sensors are likely to be increasingly contaminated by RFI as the spectrum becomes more crowded. In a previous paper we reported on a preliminary investigation of RFI observed over the United States in the 6.9-GHz channels of the Advanced Microwave Scanning Radiometer (AMSR-E) on the Earth Observing System Aqua satellite. Here, we extend the analysis to an investigation of RFI in the 6.9- and 10.7-GHz AMSR-E channels over the global land domain and for a one-year observation period. The spatial and temporal characteristics of the RFI are examined by the use of spectral indices. The observed RFI at 6.9 GHz is most densely concentrated in the United States, Japan, and the Middle East, and is sparser in Europe, while at 10.7 GHz the RFI is concentrated mostly in England, Italy, and Japan. Classification of RFI using means and standard deviations of the spectral indices is effective in identifying strong RFI. In many cases, however, it is difficult, using these indices, to distinguish weak RFI from natural geophysical variability. Geophysical retrievals using RFI-filtered data may therefore contain residual errors due to weak RFI. More robust radiometer designs and continued efforts to protect spectrum allocations will be needed in future to ensure the viability of spaceborne passive microwave sensing.

Index Terms—Advanced Microwave Scanning Radiometer (AMSR), microwave radiometry, microwave remote sensing, radio-frequency interference (RFI).

I. INTRODUCTION

RADIO-FREQUENCY interference (RFI) is an increasingly serious problem for both passive and active microwave sensing of the Earth. Man-made RFI originates from transmitters on surface, airborne, and spaceborne platforms and contaminates remote measurements of the Earth's scattering and emission by adding spurious noise of unpredictable characteristics. This is a serious concern, particularly for passive sensing, since the desired passive geophysical signals are embedded in the Earth's relatively weak thermal emission which can easily be obscured by strong RFI signals. For this reason, passive sensors

are designed to operate preferentially within protected frequency bands allocated exclusively to passive sensing. Operation of transmitters that emit above a prescribed power level within these bands is prohibited by international regulations [1]. However, there are few such protected bands in the microwave region, and for some bands the bandwidths are very narrow. As a result, to provide the variety of geophysical measurements of which they are capable, many spaceborne passive sensors currently operate in unprotected bands, and future sensors will also need to operate in these bands. Due to the increasing utilization of the microwave spectrum by active commercial services, Earth observation by passive microwave sensing is likely to be increasingly impacted by RFI in the future.

In a previous paper [2] we provided a preliminary analysis of the magnitude and extent of RFI observed over the U.S. in the 6.9-GHz channels of the Advanced Microwave Scanning Radiometer (AMSR-E) on the Aqua satellite. In this paper we extend the analysis to an investigation of RFI in the 6.9- and 10.7-GHz AMSR-E channels over the global land domain for a one-year observation period. The AMSR-E instrument was developed by the Japan Aerospace Exploration Agency (JAXA) for observation of ocean, atmosphere, cryosphere, and land phenomena [3] and has operated on the National Aeronautics and Space Administration (NASA) Aqua satellite since May 2002 [4]. AMSR-E provides measurements of several water-related parameters for hydrology, ecology, and climate applications. Over land, measurements of soil moisture and vegetation water content are useful for weather and climate forecasting, and for monitoring floods, droughts, and ecosystem dynamics. Because our primary interest is in land observations, and most of the observed RFI originates from land-based sources, we have restricted our investigation here to the global land area. The AMSR-E frequencies, bandwidths, and other instrument characteristics are listed in Table I. According to [1] there is no bandwidth allocated to passive sensing in the AMSR-E 6.75–7.10-GHz frequency range, while within the 10.6–10.7-GHz range there is only a narrow band from 10.68–10.7 GHz allocated exclusively to passive sensing. Thus, there is potential for significant RFI contamination in the 6.9-GHz (C-band) and 10.7-GHz (X-band) AMSR-E channels.

A spectral difference method was used in [2] to investigate the RFI observed at 6.9 GHz over the U.S. The RFI was found to be widespread in both vertical and horizontal polarizations, appearing mostly near highly populated urban areas. The locations of the observed RFI were found to be persistent in time, but the magnitudes exhibited temporal and directional variability (between ascending and descending passes).

TABLE I
AMSR-E NOMINAL INSTRUMENT CHARACTERISTICS

Center frequency (GHz)	6.925	10.65	18.7	23.8	36.5	89.0
Bandwidth (MHz)	350	100	200	400	1000	3000
Sensitivity (K)	0.3	0.6	0.6	0.6	0.6	1.1
3-dB footprint (km)	75 x 43	51 x 29	27 x 16	32 x 18	14 x 8	6 x 4
Sample spacing (km)	10 x 10	10 x 10	10 x 10	10 x 10	10 x 10	5 x 5
Integration time (ms)	2.5	2.5	2.5	2.5	2.5	1.2
Main-beam efficiency (%)	95.1	94.8	95.8	94.8	93.9	94.0
Beamwidth (deg)	2.2	1.5	0.8	0.92	0.42	0.19
Antenna diameter (m)	1.6					
Scan period (s)	1.5					
Antenna offset angle (deg)	47.5					
Earth-incidence angle (deg)	55					
Orbit altitude (km)	705					
Swath width (km)	1445					
Orbit type	Sun-synchronous, 1:30 pm equator crossing					
Orbit period (min)	98.8					
Sub-spacecraft velocity (km s^{-1})	6.76					

Strong and moderate RFI at 6.9 GHz could be identified using an RFI index derived from the difference between the brightness temperatures at 6.9 and 10.7 GHz. Weak RFI could not be easily distinguished, however, from brightness temperature signals caused by natural geophysical variability. This presents a difficulty in the design of robust geophysical retrieval algorithms for which RFI-contaminated data must be identified and rejected.

Different approaches have been evaluated for deriving land surface parameters from C-band AMSR-E and other passive satellite data [5]–[9]. The algorithms were designed to use the C-band frequency in preference to the higher frequencies of these sensors to maximize vegetation and soil penetration and minimize atmospheric effects. Due to the high levels of RFI observed by AMSR-E at 6.9 GHz, the current AMSR-E soil moisture retrievals use only the 10.7-GHz and higher frequencies [2], [8]. This has the disadvantage that eliminating the 6.9-GHz channels reduces the algorithm sensitivity to soil moisture (reduced vegetation and soil penetration) thereby potentially reducing the accuracy of the global soil moisture retrievals. In this paper we have explored the use of spectral difference statistics (means and standard deviations) to identify and map RFI-contaminated data on a global basis. If a reliable RFI filter or mask could be developed, this would allow use the of both 6.9- and 10.7-GHz data in areas of the globe where there is likely to be little or no RFI.

In Section II we describe the processing of the AMSR-E data used in this study. In Section III we describe the indices used to identify and characterize RFI in the AMSR-E channels, and discuss their spatial and temporal features. Section IV provides results of RFI classifications using these indices. In Section V, conclusions and implications for future work are discussed.

II. DATA AND PROCESSING

The AMSR-E instrument and its calibration are described in [3]. Calibrated and registered brightness temperatures and geophysical data products are produced by the Aqua/AMSR-E processing system in two steps from the AMSR-E level 1A instrument data provided by JAXA. First, level 2A data calibration and resolution matching is performed at Remote Sensing Systems (RSS) in Santa Rosa, CA [10]. Second, level 2B and higher geophysical retrievals are performed at the Global Hydrology and Climate Center, Huntsville, AL. The resulting data products are archived and made available to the public through the NSIDC Distributed Active Archive Center (DAAC) in Boulder, Colorado. In the level 2A processing an empirical calibration correction is applied by RSS to remove biases caused by uncertainty in knowledge of the on-orbit hot calibration reference temperature. The correction involves inferring the effective temperature of the hot calibration reference using a real-time database of operational satellite measurements acquired over the ocean [11]. The calibration includes a nonlinear correction to the 6.9-GHz brightness temperatures to adjust for a bias of approximately 7 K observed over warm land targets [12]. The current version of the archived AMSR-E level 2A data, with these calibration corrections applied, is designated version B01.

A special level 2A dataset was produced for the investigation in this paper. The processing of this dataset is identical to that of the archived version B01 level 2A data except in the treatment of extreme values. The B01 data processing indicates by flags (sets to zero) observations that exceed brightness temperatures of 330 K. The rationale is that natural Earth emissions are not expected to produce such high values, and these should therefore be rejected as erroneous in subsequent processing. For our RFI investigation, a modified level 2A dataset was generated that retained all observations, so that RFI-contaminated values could be investigated more fully. Both the B01 data and our modified data use a zero value to flag erroneous brightness temperatures that arise from other, non-RFI causes, e.g., bad or missing calibration or engineering data. These zero values are not included in subsequent processing. Regardless of the processing conventions, the AMSR-E instrument does truncate brightness temperatures that saturate the range of the analog to digital (A/D) converters, and assigns such brightness temperatures their saturation value. The brightness temperature level at which this

occurs is not fixed, but depends on the gain of each channel receiver at the time of each observation. Such brightness temperatures could be in excess of 500 K for very strong RFI contamination, but these occurrences are rare in the AMSR-E data. No residual effects from saturation in adjoining pixels have been observed in the data.

Six RFI-sensitive spectral difference indices (differences between brightness temperatures at different frequencies for a given polarization) were computed from the modified level 2A brightness temperatures. Four indices were computed from Resolution 1 data as follows: 1) $RI_{6V} = TB_{6V} - TB_{10V}$; 2) $RI_{6H} = TB_{6H} - TB_{10H}$; 3) $RI_{10V} = TB_{10V} - TB_{18V}$; 4) $RI_{10H} = TB_{10H} - TB_{18H}$ The subscripts refer to the frequency, as listed in Table I, and polarization (i.e., TB_{6V} is the brightness temperature at 6.9-GHz vertical polarization). Resolution 1 refers to the resolution of the 6.9-GHz footprint, to which all higher frequency brightness temperature data are degraded and coregistered in the level 2A processing prior to forming the indices [10]. This ensures that brightness temperatures observed at different frequencies are referenced to approximately the same spatial surface area. Two of the Resolution 1 indices, RI_{10V} and RI_{10H}, were also computed at Resolution 2 (10.7-GHz footprint resolution) for a total of six indices. The six indices (referred to here as observations) were computed from the modified level 2A swath data and accumulated in spatial bins of 0.25° latitude and longitude to form daily global arrays of data. The binned data arrays were accumulated separately for ascending and descending passes for each day. In each bin the number of observations, the sum of the observations, and the sum of squares of the observations were accumulated. The daily arrays for a given month were summed to produce monthly arrays, and twelve monthly arrays were summed to produce an annual array. The means and standard deviations at each location, for the monthly and annual time periods, were computed from the sums and sums of squares of the observations. Over one year, the number of observations in a single spatial bin is on the order of 2200 near the Equator with an increasing number at higher latitudes. The data analyzed represent one full year beginning with June 2002 and ending with May 2003.

III. RFI Characteristics

The rationale for using the spectral difference indices RI_{6V} and RI_{6H} to characterize RFI in the 6.9-GHz AMSR-E data was provided in [2]. The brightness temperatures of most land surfaces are higher at 10.7 GHz than at 6.9 GHz since the dielectric properties of water in soils and vegetation give rise to a general increase in surface emissivity with frequency in this range, resulting in negative values for RI_{6V} and RI_{6H}. Large, positive values of RI_{6V} and RI_{6H} therefore appear anomalous and may indicate the likely presence of RFI at 6.9 GHz. However, volume and surface scattering can cause the surface emissivity to decrease with increasing frequency in some cases. Thus, for example, where scattering effects dominate over absorption, such as dry snow and ice, and some desert regions, the spectral difference indices can become positive, and these regions can be interpreted erroneously as having RFI. Also, particularly for dry,

low-absorbing media, different frequencies sample the physical temperature in the medium at significantly different depths, contributing additional possible ambiguity in interpretation of the spectral differences. It is therefore desirable to find additional discriminators to achieve a more definitive characterization of RFI. In this paper we investigate the use of both the means and standard deviations of the spectral differences, and their temporal variabilities, to identify possible RFI. The rationale for the use of standard deviations as additional discriminators is that RFI originates from point sources which often have pulsed or intermittent characteristics, leading to higher standard deviations in binned brightness temperatures than would be caused by natural geophysical variability (depending on the space-time bin window). Additionally, point sources typically have directional antennas, which can lead to higher observed standard deviations due to variations in the conical scanning and day-to-day orbital viewing geometry of AMSR-E.

Global distributions of the mean and standard deviation of the RI_{6V} index for the month of July 2002 are shown in Fig. 1 for ascending (daytime) data. Also shown is the standard deviation distribution for January 2003. Strong RFI at 6.9 GHz stands out as red areas of high positive mean values, and high standard deviations, most noticeable in the United States, the Middle East, and Japan, with additional locations in Europe, Asia, South America, and Africa. Some areas show high positive mean values but low standard deviations, such as the Antarctic. A few regions such as Greenland have mixed standard deviations, while others such as England and Italy have high negative mean values and high standard deviations. Fig. 2 shows the regional distributions over Europe of the means and standard deviations of the RI_{6V} and RI_{10V} indices. These maps show high positive mean values and high standard deviations of RI_{10V} in England and Italy. This feature is also observed in Japan (not shown) and can be interpreted as RFI at 10.7 GHz. From these observations it is apparent that RFI at either 6.9 or 10.7 GHz can be identified by classifying locations that show large magnitudes of both means and standard deviations of RI_{6V} or RI_{10V}. Misclassification could occur if RFI of similar magnitude is observed when viewing a given location at both 6.9 and 10.7 GHz. (The antenna pattern can also influence the classification characteristics, as discussed in Section IV.) Ambiguity also arises in regions where time-varying geophysical phenomena, with correspondingly large time-varying brightness temperature signatures, cause high standard deviations at the monthly time scale, that can be confused with RFI. This occurs, for example, with melting in the Greenland ice sheets in summer, as seen in the large standard deviations over Greenland in Fig. 1(b). This feature is not present in winter, as indicated by the low standard deviations for the same region seen in Fig. 1(c). To eliminate such ambiguity it is necessary to examine time-sequences of the statistics, to distinguish between the different variability time scales of RFI and naturally occurring geophysical processes. Another feature, evident particularly in the regional view of Fig. 2, is the effect of the AMSR-E spatial footprint on the binned values near coastlines, particularly the standard deviations. A coastline mask has been applied to remove ocean and large inland water regions. However, land brightness temperatures near the coastlines are influenced
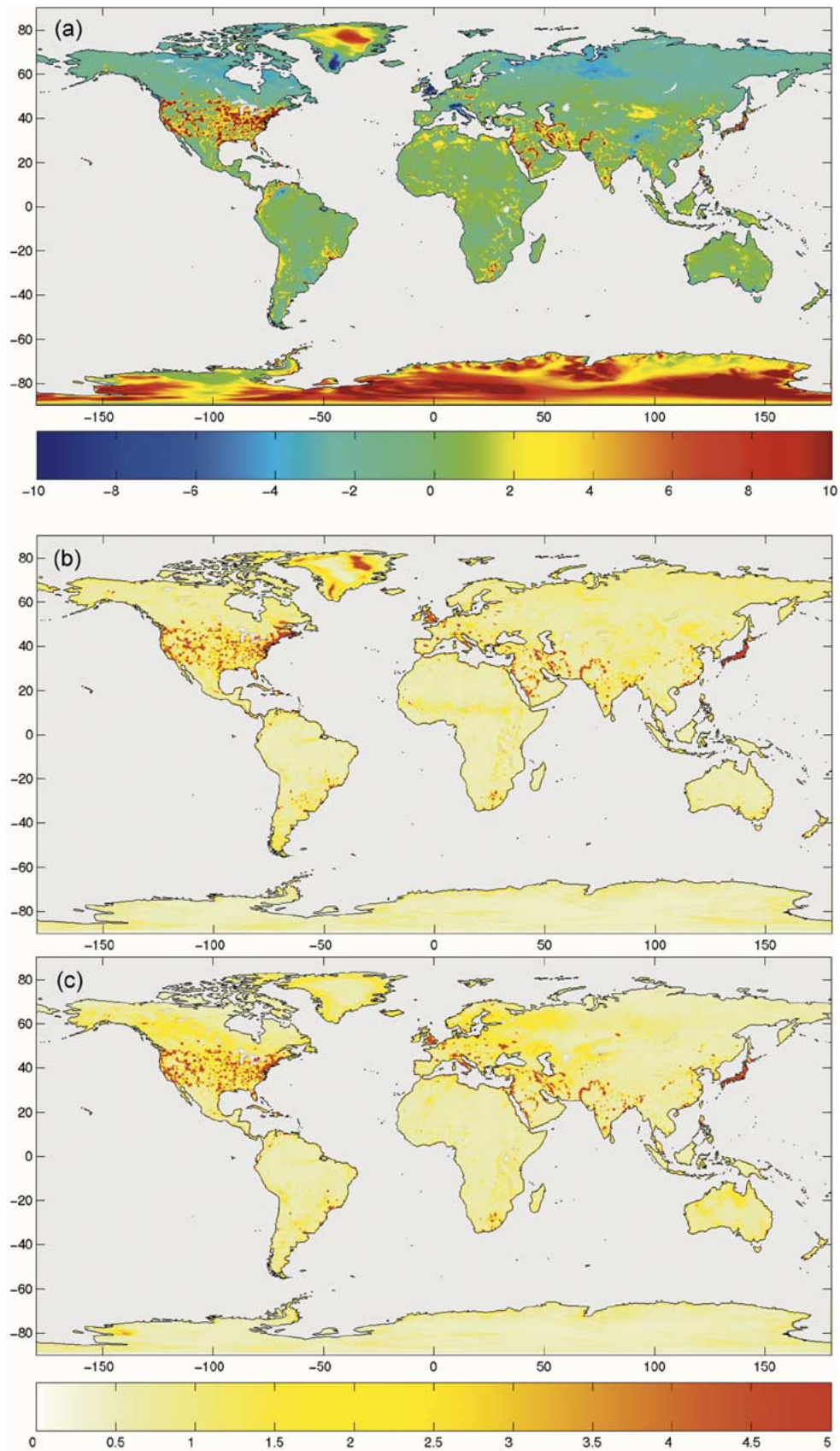
Fig. 1. Global maps of (a) means and (b) standard deviations of AMSR-E brightness temperature spectral difference $(RI_{6V} = TB_{6V} - TB_{10V})$ for July 2002. Standard deviations for January 2003 are shown in (c). The statistics are derived by aggregating data within $0.25°$ latitude and longitude bins. Color scale units are in Kelvins.

by ocean emission viewed in the antenna sidelobes. This effect can be removed from consideration by masking the pixels bor-

dering the coastlines. The effects are directional and, for the data shown in Fig. 2, are related to the inclination of the as-
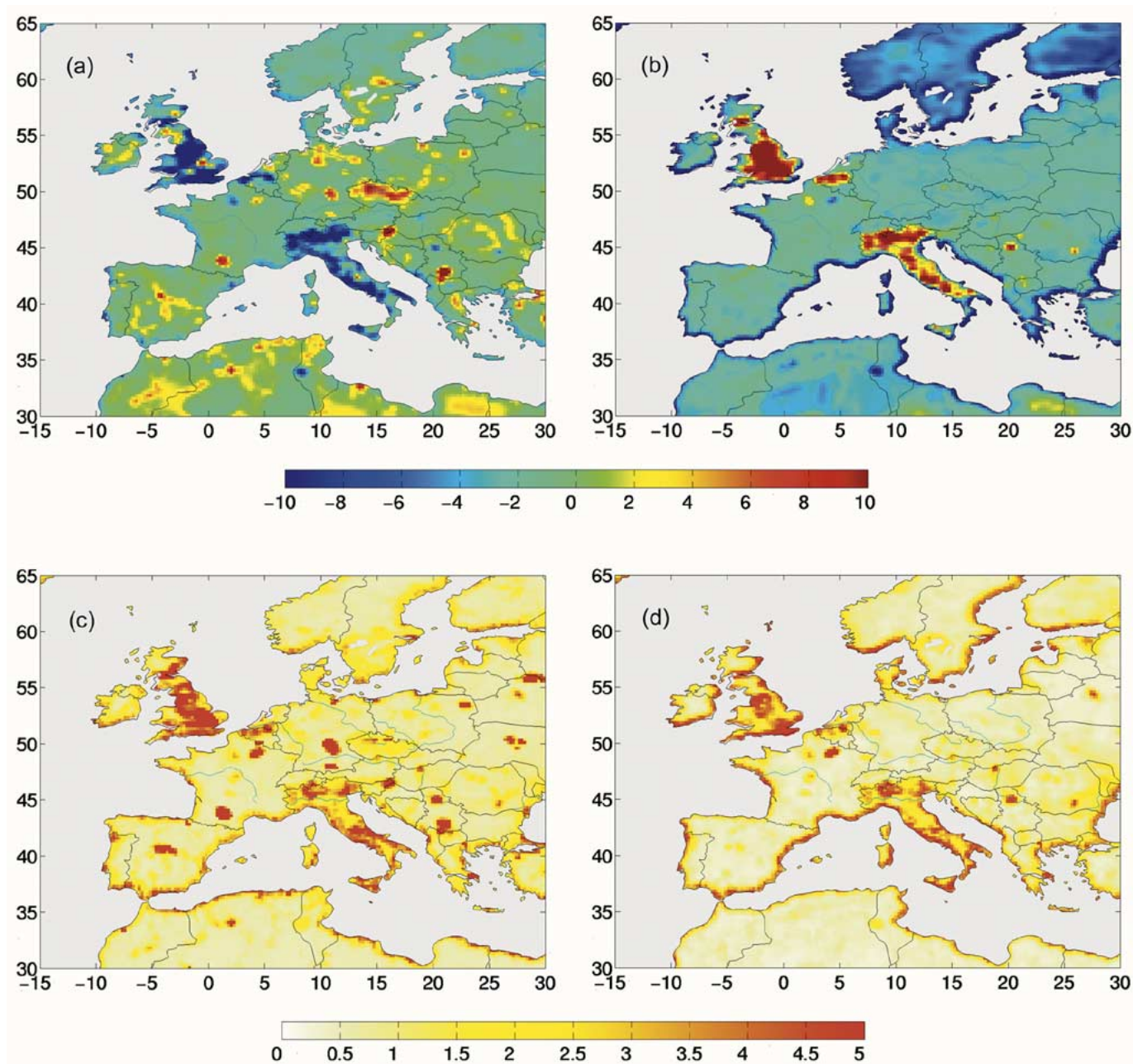
Fig. 2. Regional maps of means and standard deviations of AMSR-E brightness temperature spectral differences $RI_{6V} = TB_{6V} - TB_{10V}$ and $RI_{10V} = TB_{10V} - TB_{18V}$ for July 2002. (a) RI_{6V} mean, (b) RI_{10V} mean, (c) RI_{6V} standard deviation, (d) RI_{10V} standard deviation. The statistics are derived by aggregating data within $0.25°$ latitude and longitude bins. Color scale units are in Kelvins.

cending swaths. Geolocation bias errors, if any, could also be a contributing factor.

At this stage it is useful to consider two types of RFI identification objectives. The first is to identify the locations of all apparent RFI sources observed globally, based on long term statistics. The second is to identify RFI at a given location and time, as part of the real-time satellite data processing, where instantaneous identification and rejection of bad data is necessary for accurate retrieval of geophysical parameters (such as soil moisture). The first objective can be addressed by analyzing data over an annual cycle, carefully separating the signatures of RFI sources from the natural background variability, and deriving a one-time "mask" of RFI locations. Once derived, such a mask can be used for the second objective, but this mask

would not capture possible new RFI sources that might originate after the mask was created, or could be overconservative in permanently masking out locations that may have brief or infrequent RFI.

To develop the classification approach and examine the temporal RFI variability, two-dimensional (2-D) histograms were constructed of the means (μ) and standard deviations (σ) of RI_{6V} and RI_{10V} within each $0.25°$ latitude-longitude bin, for two regions: "global," and "Europe." No particular significance is placed on the choice of Europe as a region for study other than its diversity of terrain and national boundaries. "Global" refers to the global land area, excluding regions of permanent snow and ice (e.g., Greenland and Antarctica). "Europe" refers to the region shown in Fig. 2, which also includes part of north
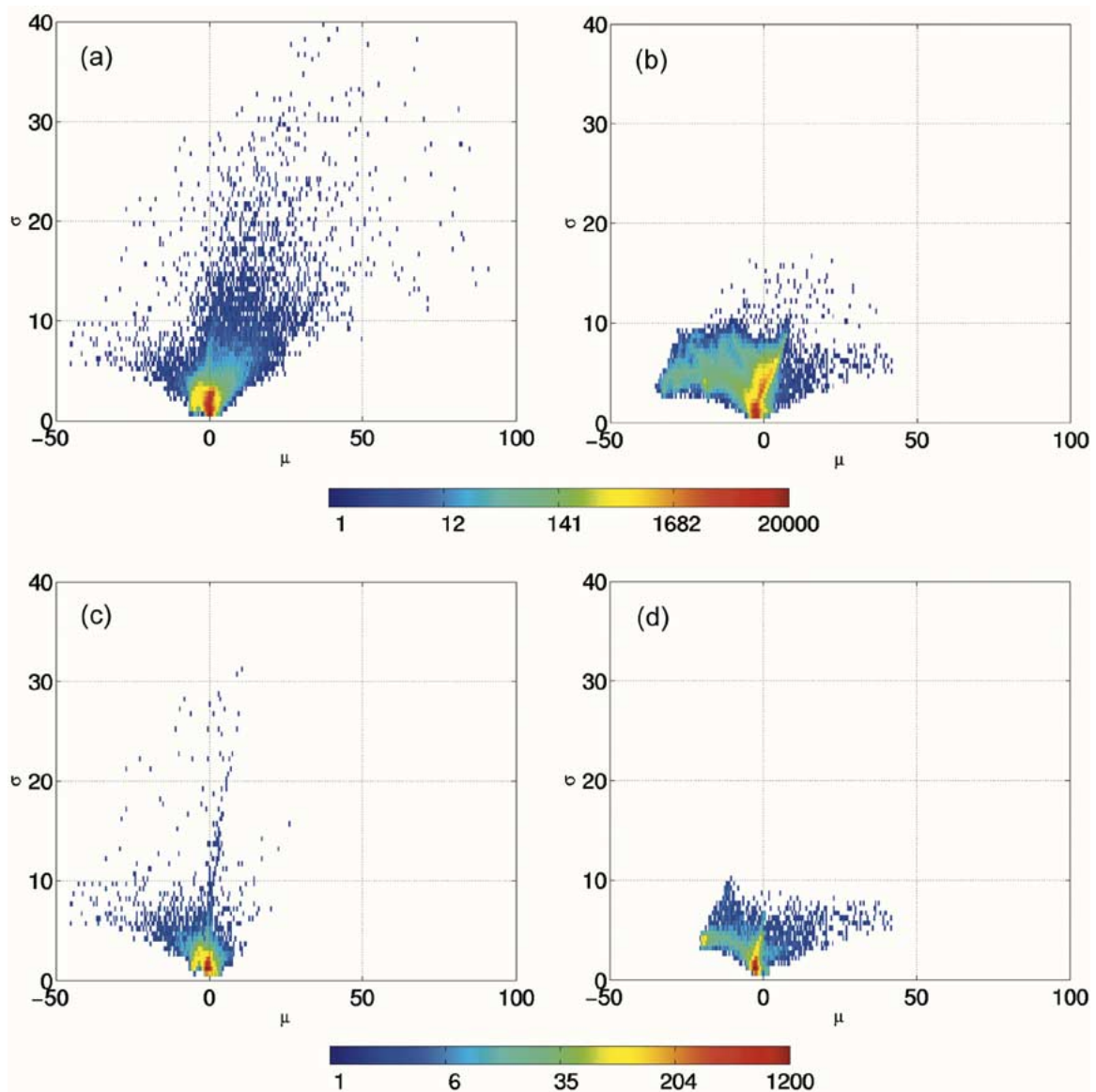
Fig. 3. Two-dimensional histograms of $RI_{6V} = TB_{6V} - TB_{10V}$ and $RI_{10V} = TB_{10V} - TB_{18V}$, combining data from all months for the year June 2002 through May 2003. (a) RI_{6V} global, (b) RI_{10V} global, (c) RI_{6V} Europe, and (d) RI_{10V} Europe. The global region excludes oceans and permanent ice. The Europe region is shown in Fig. 2. The vertical axis is the standard deviation, and the horizontal axis is the mean. The color scale indicates the number of points (logarithmic) within each 0.5-K increment of mean and standard deviation.

Africa. The histograms are shown in Figs. 3 and 4. The majority of points are clustered within a few Kelvins of the intersection of the $\mu = 0$ and $\sigma = 0$ axes. Data values far from this intersection are indicative of RFI contamination. The RI_{10V} histograms show much less dispersion in the standard deviations than those of RI_{6V}, indicating the lower prevalence of RFI at 10.7 GHz. The greater dispersion in the means of RI_{10V} relative to RI_{6V} is contributed to by the greater effects of time-varying geophysical features on RI_{10V}. To illustrate the time-variability of the monthly mean and standard deviation statistics Fig. 4 shows monthly 2-D histograms of the means and standard deviations of RI_{6V} spaced four months apart, i.e., September 2002, January 2003, and May 2003. The general shape of the histograms is similar for all months, though close inspection of the histogram mean values reveals small trends as a function of time. These trends are shown in Fig. 5(a) in which global averages of the

RI_{6V} and RI_{10V} means and standard deviations are plotted for each month. A similar plot is shown in Fig. 5(b) for the Europe region. Seasonal trends are evident, particularly in the means. There are regional differences also, as illustrated by the different levels and trends observed for Europe versus the global region. The seasonal trends are most likely related to geophysical variability, since there is no reason to expect RFI to show such trends. The standard deviations are more stable temporally and spatially than the means.

IV. RFI CLASSIFICATION

The time-variability exhibited in Fig. 5 suggests that fixed threshold values of μ and σ may not provide consistent RFI classifications for all regions and seasons, particularly if discrimination of weak RFI is desired. In this case, temporally and spa-
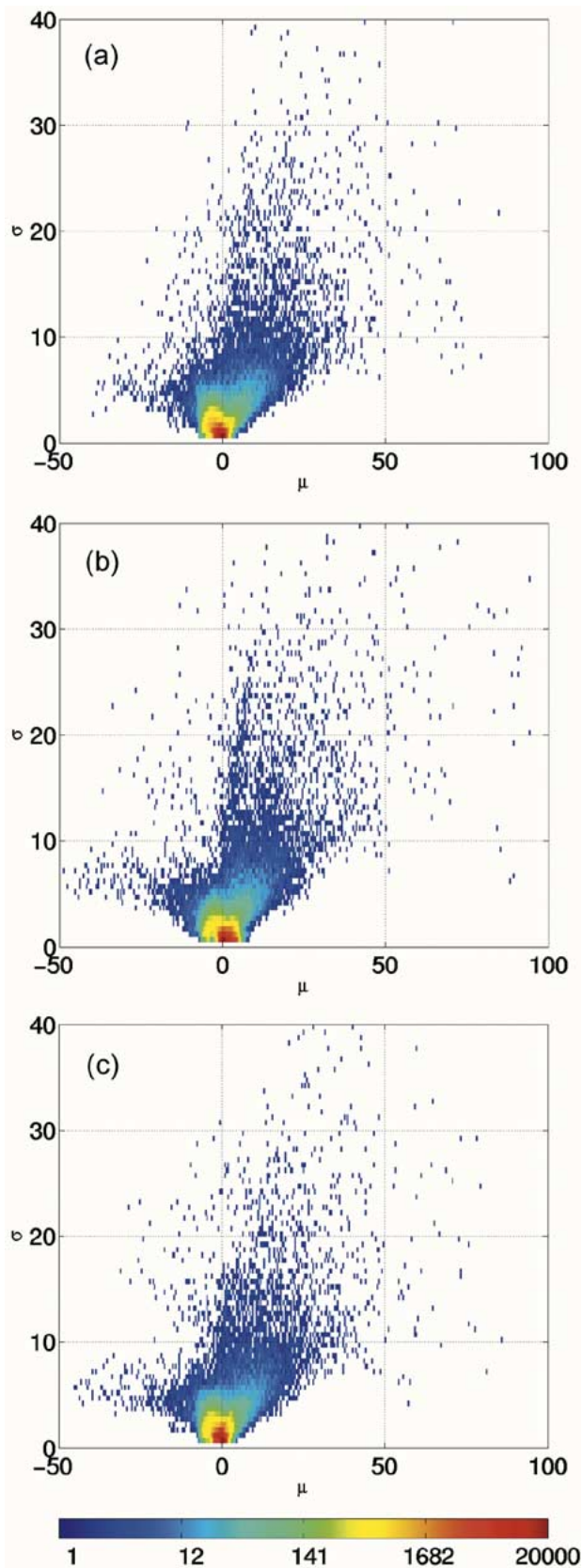
Fig. 4. Monthly 2-D histograms of the means and standard deviations of $RI_{6V} = TB_{6V} - TB_{10V}$ for (a) September 2002, (b) January 2003, and (c) May 2003, for the global region (excluding oceans and permanent snow and ice). The vertical axis is the standard deviation (σ), and the horizontal axis is the mean (μ). The color scale indicates the number of points (logarithmic) within each 0.5-K increment of mean and standard deviation.
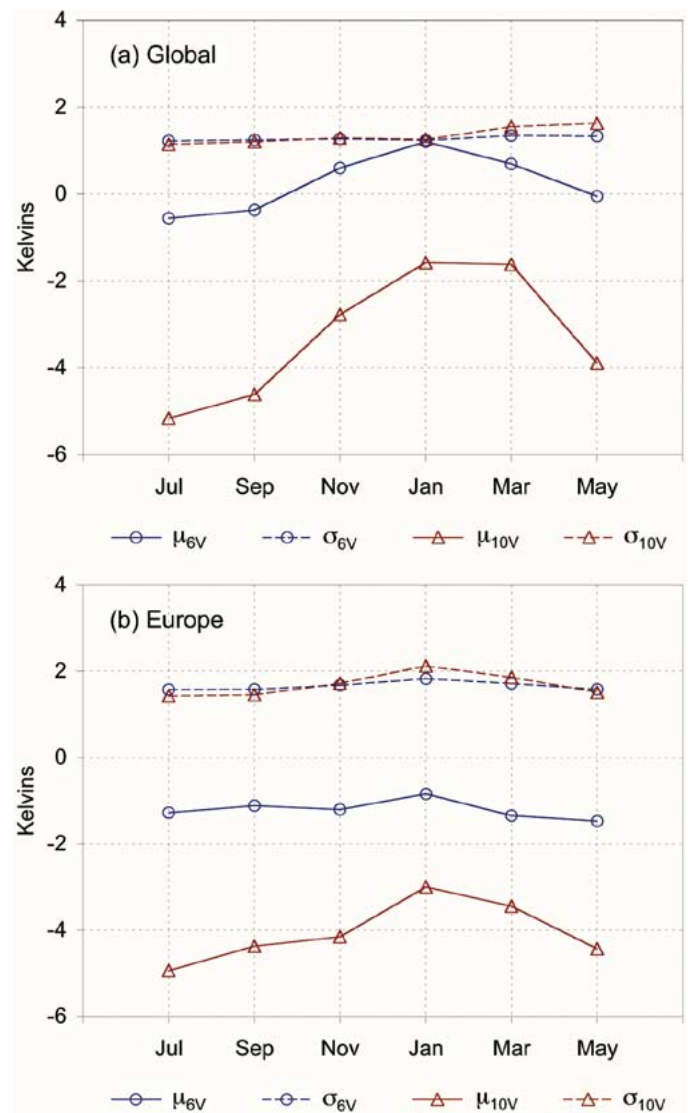
Fig. 5. Monthly variations of the means (μ) and standard deviations (σ) of RI_{6V} and RI_{10V}, averaged (a) over the globe and (b) over Europe.

tially varying thresholds may need to be determined for more specificity. The selection of thresholds is subjective since there are no natural breakpoints in the histograms of Figs. 3 and 4 that would suggest a clear distinction. On the other hand, moderate to strong RFI, as evidenced by high values of μ and σ, can be masked by thresholding. Fig. 6 shows maps of moderate to strong RFI locations for July 2002 estimated using thresholds of $\mu = 3$ K and $\sigma = 3$ K for RI_{6V}, and $\mu = -0.25$ K and $\sigma = 3$ K for RI_{10V}. These thresholds were chosen by subjective inspection of the curves in Fig. 5 for illustration purposes. Fig. 6(a) shows the RFI locations at 6.9 GHz, while Fig. 6(b) shows the locations at 10.7 GHz. The equivalent global maps are shown in Fig. 7. These maps can be compared with Figs. 1 and 2, and show more clearly the estimated extent of RFI. The RFI observed at 6.9 GHz is relatively sparse and scattered in Europe, while at 10.7 GHz it is more densely concentrated in England and Italy. On the global scale, the 6.9-GHz RFI is most densely concentrated in the U.S., the Middle East, and Japan, while at 10.7 GHz the RFI is concentrated mostly in England, Italy, and Japan. It should be emphasized that these classified
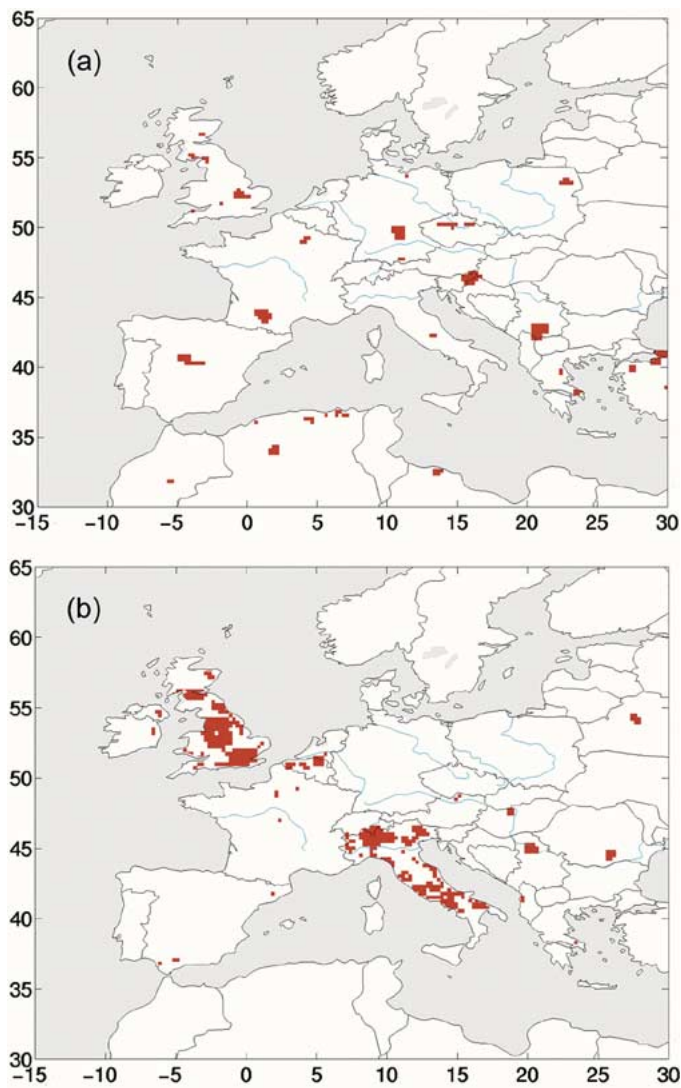
Fig. 6. Classification maps of RFI over Europe. (a) 6.9-GHz RFI using thresholds of $\mu = 3$ K and $\sigma = 3$ K. (b) 10.7-GHz RFI using thresholds of $\mu = -0.25$ K and $\sigma = 3$ K.

Fig. 7. Classification maps of global RFI. (a) 6.9-GHz RFI using thresholds of $\mu = 3$ K and $\sigma = 3$ K. (b) 10.7-GHz RFI using thresholds of $\mu = -0.25$ K and $\sigma = 3$ K.

RFI locations are estimates only, based on inferences from the satellite data, and have not been verified by comparisons with other information such as locations and radiating characteristics of known ground transmitters. Such comparisons are being considered elsewhere [13].

Classification maps such as Figs. 6 and 7 can be used to generate masks for rejecting contaminated AMSR-E data at 6.9 and 10.7 GHz. By masking the locations of known or suspected RFI, the use of these channels for generating soil moisture and vegetation retrievals on a global scale can be made more reliable and productive. It is possible to refine the masks by using time-varying thresholds derived from curves such as in Fig. 5. Such thresholds could compensate for seasonal variations in RFI-free geophysical signals. The threshold fine-tuning could also be made region and surface specific. Fundamentally, the issue for land geophysical retrievals is balancing the tradeoff between allowing too much RFI-contamination (by using too loose an RFI threshold) and removing more of the land area than necessary due to suspected but nonexistent RFI (by using too tight a threshold).

The above discussion has focused on the two indices RI_{6V} and RI_{10V} at Resolution 1. As discussed earlier, six indices were computed and analyzed. It was found that differences between the RI_{10V} and RI_{10H} indices calculated at Resolution 1 and Resolution 2 were small. It was also found that the V-polarized indices provided somewhat better RFI discrimination than the H-polarized indices, due to the greater influence of geophysical variability on the H-polarized brightness temperatures at the AMSR-E incidence angle ($\sim 55°$). In the earlier study [2] some differences were observed in the polarizations of the RFI sources, however, this was not investigated further here. Since many of the RFI locations observed within the AMSR-E antenna footprint may contain several point sources, the footprint-integrated RFI most often appears strongly in both polarizations. Some differences are observed between RFI maps generated using ascending and descending data. This could be due to the different viewing azimuths of the antenna for ascending versus descending passes, and the different times of day for the ascending and descending passes. In general, however, the classified RFI maps using ascending or descending passes, and V or H data, appear quite similar.

The resolution and accuracy of the RFI index and classification maps are influenced by the antenna pattern characteristics and the data binning procedure. As discussed earlier, for our study the level 2A data were binned on a 0.25° latitude-longitude grid. However, the spatial resolution of the level 2A data is determined by the antenna 3-dB beamwidth (Table I), which at 6.9 GHz yields an elliptical footprint (75 km × 43 km) that is much larger than 0.25° latitude-longitude when projected at the surface. Furthermore, only about 50% of the received power

comes from within the 3-dB beamwidth, while about 95% of the power is received from within the main beam defined as 2.5 times the 3-dB beamwidth. (Outside the main beam, the highest side-lobe is about 28 dB down from the boresight (beam axis) level, though the beam shape and sidelobe patterns exhibit significant azimuthal asymmetry [3]. There is also asymmetry at the surface as a function of antenna scan angle due to the changing orientation of the elliptical projection of the beam at the surface.) It is possible that a strong RFI source could influence the AMSR-E measurement up to a few footprints or more from the viewing boresight. The magnitude of the influence would depend on the azimuth viewing angle, which varies at different positions in the swath and for ascending versus descending orbits. Quantification of these effects is beyond the scope of this paper, but would be useful for a more in-depth analysis.

V. CONCLUSION

In this paper we have surveyed the global extent of RFI in the AMSR-E 6.9 and 10.7-GHz channels, and have considered the feasibility of identifying and masking RFI locations to enhance geophysical retrievals over land. Of the six indices studied, RI_{6V} and RI_{10V} provide the best combined information for this purpose, and we have used these indices to illustrate spatial and temporal features of the AMSR-E observed RFI. Classifications using these indices appear to be robust in identifying strong and persistent RFI. However, identifying weak RFI remains a problem, and is unlikely to be solved by examining satellite data alone. Better discrimination can be obtained by deriving classification thresholds that vary spatially and temporally. The use of spectral indices implies that the geophysical signature of these indices is reasonably well known *a priori*, as a background against which to detect RFI. However, *a priori* knowledge of this signature would imply that there is little added information in the use of both channels over a single channel for geophysical retrieval. We have found that the standard deviations of the indices are more temporally stable than the means of the indices due to geophysical variability. The standard deviations may therefore provide better discrimination of RFI than the means. In this paper, we have used the standard deviations and the means in combination, in the absence of a reliable validation dataset of "true" RFI against which to evaluate the merits of different classification schemes.

ACKNOWLEDGMENT

REFERENCES

[1] ITU, *Radio Regulations*. Geneva, Switzerland: International Telecommunications Union, 2001.

[2] L. Li, E. Njoku, E. Im, P. Chang, and K. S. Germain, "A preliminary survey of radio-frequency interference over the U.S. in Aqua AMSR-E data," *IEEE Trans. Geosci. Remote Sens.*, vol. 42, no. 2, pp. 380–390, Feb. 2004.

[3] T. Kawanishi, T. Sezai, Y. Ito, K. Imaoka, T. Takeshima, Y. Ishido, A. Shibata, M. Miura, H. Inahata, and R. Spencer, "The Advanced Microwave Scanning Radiometer for the Earth Observing System (AMSR-E), NASDA's contribution to the EOS for global energy and water cycle studies," *IEEE Trans. Geosci. Remote Sens.*, vol. 41, no. 2, pp. 184–194, Feb. 2003.

[4] C. L. Parkinson, "Aqua: An earth-observing satellite mission to examine water and other climate variables," *IEEE Trans. Geosci. Remote Sens.*, vol. 41, no. 2, pp. 172–183, Feb. 2003.

[5] E. Njoku and L. Li, "Retrieval of land surface parameters using passive microwave measurements at 6–18 GHz," *IEEE Trans. Geosci. Remote Sens.*, vol. 37, no. 1, pp. 79–93, Jan. 1999.

[6] S. Paloscia, G. Macelloni, E. Santi, and T. Koike, "A multifrequency algorithm for the retrieval of soil moisture on a large scale using microwave data from SMMR and SSM/I satellites," *IEEE Trans. Geosci. Remote Sens.*, vol. 39, pp. 1655–1661, 2001.

[7] M. Owe, R. De Jeu, and J. Walker, "A methodology for surface soil moisture and vegetation optical depth retrieval using the microwave polarization difference index," *IEEE Trans. Geosci. Remote Sens.*, vol. 39, pp. 1643–1654, 2001.

[8] E. Njoku, T. Jackson, V. Lakshmi, T. Chan, and S. Nghiem, "Soil moisture retrieval from AMSR-E," *IEEE Trans. Geosci. Remote Sens.*, vol. 41, no. 2, pp. 215–229, Feb. 2003.

[9] N. Chauhan, S. Miller, and P. Ardanuy, "Spaceborne soil moisture estimation at high resolution: a microwave-optical/IR synergistic approach," *Int. J. Remote Sens.*, vol. 24, pp. 4599–4622, 2003.

[10] P. Ashcroft and F. Wentz, "Algorithm theoretical basis document (ATBD): AMSR level 2A algorithm," Remote Sensing Systems, Santa Rosa, CA, RSS Tech. Rep. 121 599B-1, 2000.

[11] F. J. Wentz, C. Gentemann, and P. Ashcroft, "On-orbit calibration of AMSR-E and the retrieval of ocean products," Remote Sensing Systems, Santa Rosa, CA, [Online]. Available: http://www.ssmi.com/amsr/amsr_data_description.html, 2003.

[12] E. Njoku, T. Chan, W. Crosson, and A. Limaye, "Evaluation of the AMSR-E data calibration over land" (in English), *Rivista Ital. Telerilevamento (Ital. J. Remote Sens.)*, vol. 30/31, pp. 19–37, 2004.

[13] D. Kunkee, private communication, 2004.

Eni G. Njoku (M'77–SM'83–F'95) received the B.A. degree in natural and electrical sciences from Cambridge University, Cambridge, U.K., in 1972, and the M.S. and Ph.D. degrees in electrical engineering from the Massachusetts Institute of Technology, Cambridge, in 1974 and 1976.

He is currently a Principal Scientist with the Jet Propulsion Laboratory (JPL), Pasadena, CA, and is the JPL Project Scientist for the HYDROS mission. From 1976 to 1977, he was a National Research Council Resident Research Associate. In 1977, he joined JPL. From 1986 to 1990, he served as Discipline Scientist for Ocean and Earth Science Data Systems at NASA Headquarters, Washington, DC, and from 1993 to 1994, he was Manager of the Geology and Planetology Section at JPL. During the 2001–2002 academic year, he was on leave as a Visiting Professor at the Massachusetts Institute of Technology. He is a member of the Aqua Advanced Microwave Scanning Radiometer science team and was Principal Investigator for the IIP OSIRIS technology study. His primary interests are in the use of passive and active microwave remote sensing for hydrology and climate applications. His research involves studies of microwave interactions with land surfaces and retrieval algorithm development.

Dr. Njoku is a member of the American Meteorological Society, the American Geophysical Union, the American Association for the Advancement of Science, Commission F of the International Union of Radio Science, and Sigma Xi. He has served as an Associate Editor of the IEEE TRANSACTIONS ON GEOSCIENCE AND REMOTE SENSING (1985–1988) and was the Technical Program Chairman for IGARSS'94 held in Pasadena, CA. He has been a recipient of NASA Group Achievement Awards in 1980, 1982, and 1985, and he was awarded the NASA Exceptional Service Medal in 1985.

Peter Ashcroft received the B.S. degree in applied physics from the California Institute of Technology, Pasadena, in 1986, and the Ph.D. degre from Carnegie Mellon University (CMU), Pittsburgh, PA, writing his doctoral dissertation on the relative merits of ground-, air-, and space-based methods for characterization of methane sources on the surface.

From 1986 to 1988, he was with Lockheed Missiles and Space Corporation, Sunnyvale, CA. He joined Remote Sensing Systems (RSS) Santa Rosa, CA, in November of 1995. Since then, he has worked on spatial resampling of microwave radiometer observations (for the AMSR-E and Midori AMSR instruments), data processing and format issues for AMSR-E, and calibration questions for both the TMI and AMSR-E instruments. Recent investigations of radio-frequency interference in sensing data are an outgrowth of ongoing AMSR-E calibration work.

Tsz K. Chan (M'02–SM'03) received the B.S. degree in electrical engineering from Portland State University, Portland, OR, in 1993, and the M.S. and Ph.D. degrees in electrical engineering from the University of Washington, Seattle, in 1995 and 1998, respectively.

From June 1998 to February 1999, he was a Research Associate at the University of Washington, where he developed experimental techniques for microwave confocal imaging and subsurface sensing of concealed objects embedded in random media. In 1999, he joined NASA Jet Propulsion Laboratory (JPL), Pasadena, CA, as a Caltech Postdoctoral Scholar. At JPL, he is now responsible for algorithm development of soil moisture retrieval for the Advanced Microwave Scanning Radiometer instrument on the NASA EOS Aqua satellite. Currently, he is a Scientist of the Terrestrial Sciences Research Element at JPL.

Li Li (M'96) received the M.S. degree from Beijing University of Posts and Telecommunications, Beijing, China, and the Ph.D. degree from the University of Washington, Seattle, in 1987 and 1995, respectively, both in electrical engineering.

He is currently with the Naval Research Laboratory, Washington, DC, working on algorithm development for the spaceborne polarimetric microwave radiometer onboard the WindSat satellite. From 1997 to 2004, he was with the Jet Propulsion Laboratory, California Institute of Technology, Pasadena, where he participated in several NASA projects, including the land algorithm development for Aqua Advanced Microwave Scanning Radiometer (AMSR-E), sensor calibration and Level 1B processing for the CloudSat Cloud Profiling Radar (CPR), TRMM cross-sensor calibration and data analysis, second-generation precipitation radar data calibration and analysis, and ocean surface latent heat flux studies. From 1995 to 1997, he was with the Caelum Research Corporation, Rockville, MD, working at the Office of Research and Applications, National Environmental Satellite, Data and Information Service, National Oceanic and Atmospheric Administration (NOAA/NESDIS), Camp Springs, MD, where he conducted research in the area of polarimetric microwave radiometry, especially for the concept study of ocean surface wind vector sensing. He was a Student Visitor from 1993 to 1995 at the National Center for Atmospheric Research, Boulder, CO. His research interests include passive and active remote sensing of land and ocean surfaces for applications related to climate study and monitoring.

Dr. Li is a member of the American Geophysical Union, the IEEE Geoscience and Remote Sensing Society, and Eta Kappa Nu. He has been a recipient of the NCAR/RAP Fellowship 1993–1995 and the NASA Group Achievement Award and JPL Technical Excellence Award, both in 2002.